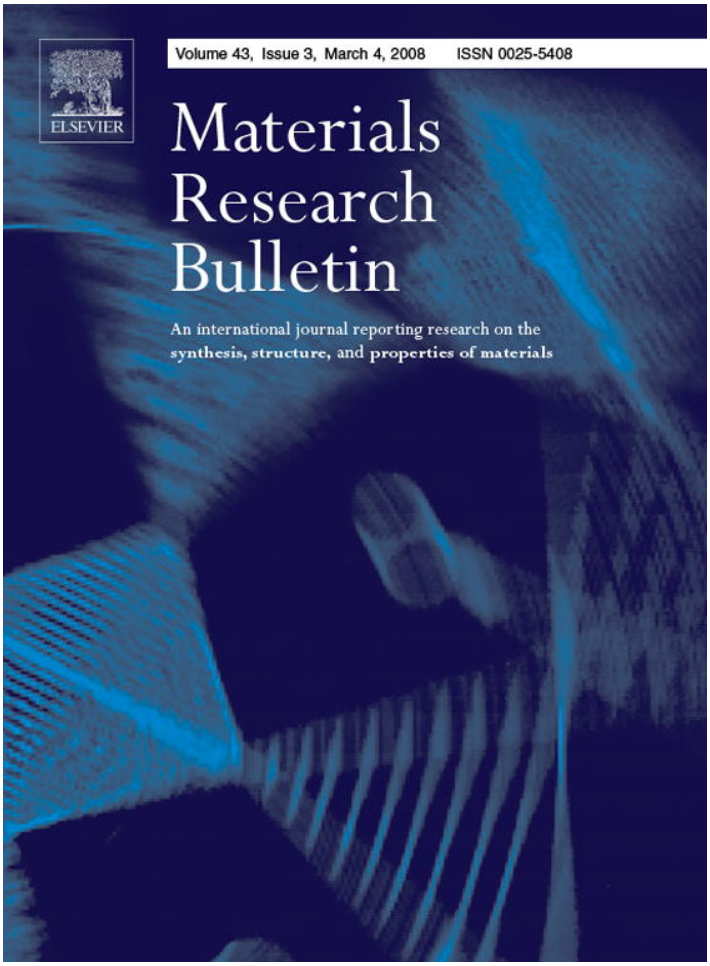

Available online at www.sciencedirect.com
ScienceDirect
Materials Research Bulletin 43 (2008) 676–681
Materials Research Bulletin
www.elsevier.com/locate/matresbu

The phase diagram YF_3–GdF_3

D. Klimm [a,*], I.M. Ranieri [b], R. Bertram [a], S.L. Baldochi [b]

[a] *Institute for Crystal Growth, Max-Born-Str. 2, 12489 Berlin, Germany*
[b] *Center for Lasers and Applications, Inst. Pesquisas Energeticas & Nucl., CP 11049, Butantã 05422-970, São Paulo, SP, Brazil*

Received 12 December 2006; received in revised form 28 March 2007; accepted 2 April 2007
Available online 8 April 2007

Abstract

The binary phase diagram YF_3–GdF_3 was studied by differential scanning calorimetry (DSC). Yttrium fluoride and gadolinium fluoride show complete miscibility in all three phases (orthorhombic room temperature phase, trigonal or hexagonal high temperature phase, liquid). The transformations between room temperature and high temperature phases are of first order and occur at 1338.6 K (YF_3) or 1174.8 K (GdF_3). Melting points are 1403.1 K (YF_3) or 1525.7 K (GdF_3), respectively. The $c_p(T)$ curve of GdF_3 shows a λ shaped local maximum at 1333 K that might be related to a further solid phase transformation of second order.

PACS : 65.40.Ba; 81.30.Dz; 81.70.Pg

Keywords: A. Fluorides; C. Differential scanning calorimetry (DSC); D. Phase equilibria

1. Introduction

Most fluorides REF_3 (RE = rare earth metal) show dimorphism. Depending on temperature T and on the RE, the REF_3 exist in an orthorhombic *Pnma* (β-YF_3), a cubic $Pm\bar{3}m$, a hexagonal $P6_3cm$ (LaF_3, tysonite), or a trigonal $P\bar{3}c1$ structure, respectively. Sometimes the space symmetry groups $P6_3/mmc$ and $P6_322$ have been reported. The REF_3 with smaller RE^{3+} (starting about at Sm^{3+} with an octahedral radius $r_{Sm} = 109.8$ pm) are reported to undergo a reconstructive phase transformation upon heating [1]. Yttrium ($r_Y = 104.0$ pm) behaves here like a small rare earth element. This phase transformation has been discussed controversially and seems to depend on the content of OH^- impurities within the material [2–5]. The transformation is not observed for large RE (La^{3+}, Ce^{3+}, Pr^{3+}, Nd^{3+}) and bulk single crystals of LaF_3, CeF_3, PrF_3, and NdF_3 can be grown from the melt without cracking [6,7].

If the radii of two $RE^{3+}$are not too different, they can replace each other in crystals and doping is possible. Up to now, most of the quasi binary systems between different REF_3 have not been investigated, although some of them are interesting examples for scintillator applications [7]. Moreover, some RE doped scheelite type crystals of the type $LiREF_4$ (e.g. $LiYF_4$) are used for lasers [8]. Such compounds are known to exist for the smaller RE^{3+}(starting about at RE = Eu). For $RE^{3+}$with RE = Eu, Gd, Tb, Dy, or Ho, respectively, the $LiREF_4$ melt incongruently. For $LiYF_4$–$LiErF_4$ both end members melt congruently and the system is quasi-binary [9]. Other compounds like $LiGdF_4$ that display

* Corresponding author. Tel.: +49 30 6392 3024; fax: +49 30 6392 3003.
E-mail address: klimm@ikz-berlin.de (D. Klimm).
URL: www.ikz-berlin.de

0025-5408/$ – see front matter
doi:10.1016/j.materresbull.2007.04.004

incongruent melting behavior may not be regarded as end members spanning quasi-binary phase diagrams. Hence, detailed knowledge on the ternary system LiF–YF_3–GdF_3 is necessary for a complete description of the section $LiYF_4$–$LiGdF_4$.

Besides the rim system LiF–GdF_3 with one intermediate phase $LiGdF_4$ melting incongruently [8], the rim system LiF–YF_3 with one intermediate compound $LiYF_4$ melting congruently was reported previously [10]. Some contrary reports claiming incongruent melting of $LiYF_4$ may result from the small difference (≈ 1 mol%) between this compound and the neighboring eutectic $LiYF_4/YF_3$. The third rim system YF_3–GdF_3 is the subject of this study.

2. Experimental

YF_3 and GdF_3 are available from different commercial suppliers (e.g. Alfa Aesar, Aldrich) with nominal purities up to 99.99%. Such chemicals were studied by simultaneous differential scanning calorimetry/thermogravimetry (DSC/TG) as described later in this study and considerable mass loss up to several percent, together with irregular melting (and sometimes even phase transformation) peaks was observed. One can assume that these effects are a result of contamination by adsorbed water that reacts with the rare earth (RE) fluoride

$$2REF_3 + 3H_2O \rightleftarrows RE_2O_3 + 6HF\uparrow \quad (1)$$

under mass loss and contamination of the remaining REF_3 with RE_2O_3. Considerably better thermoanalytic results could be obtained from fluorides that were prepared from commercial Y_2O_3 and Gd_2O_3 (5N purity) by fluoridation. The oxides were placed in a platinum boat inside a platinum tube. They were slowly heated in a stream of argon gas (White Martins, purity 99.995%) and HF gas (Matheson Products, purity 99.99%) up to 850 °C. This process is described in detail in references [11,12]. Conversion rates around 99.96% of the theoretical value calculated for the reactions $Y_2O_3 + 6\,HF \rightarrow 2\,YF_3 + 3\,H_2O$ or $Gd_2O_3 + 6\,HF \rightarrow 2\,GdF_3 + 3\,H_2O$, respectively, were measured by comparing the masses prior to and after the fluoridation process. If such pure REF_3 were intentionally mixed with RE_2O_3, irregular DSC peaks, but no mass loss was observed.

Thermoanalytic measurements were performed with a NETZSCH STA 449C ''Jupiter'' using a standard DSC/TG sample carrier (thermocouples type S) and heating/cooling rates of ± 10 K/min to ≈ 50 K above the fusion point T_f of the samples, i.e. up to 1200–1350 °C. The pure substances YF_3 and GdF_3 were investigated additionally with a c_p-DSC/TG sample carrier that allows a higher accuracy sufficient for measurements of the specific heat capacity $c_p(T)$. The sample carriers were calibrated for T and sensitivity at the phase transformation points of $BaCO_3$ and at the melting points of Zn, Au, and Ni. Sample powders (typically 20–50 mg) were placed in graphite DSC crucibles with lid. Graphite crucibles were used for two reasons: (1) graphite is not wetted by the molten fluorides. Thus the melt forms a single almost spherical drop (diameter $d \approx 2$ mm). The small surface reduces contamination and the small volume enhances effective mixing of the sample. (2) Graphite removes residual water from the atmosphere very effectively for $T \geq 1000$ °C) [13]. For the c_p measurements a commercial (NETZSCH) c_p standard made of sapphire (thickness 0.75 mm, mass 63.73 mg) was used. The specific heat capacity was calculated following the ASTM E 1269 method of the NETZSCH ''Proteus'' analysis software that compares curves from three subsequent DSC runs: (1) empty crucible, (2) crucible with sapphire standard, (3) crucible with sample.

Solid solutions $Gd_xY_{1-x}F_3$ were obtained by weighing appropriate quantities of YF_3 and GdF_3 powder directly into the crucible. Mixing was performed by a first heating run above the melting point. Usually DSC curves from the second heating run were used for analysis. This method of mixing proved to be superior to a preceding treatment e.g. in a mortar, as the fluorides are known to be highly sensitive to traces of water in the atmosphere. The sample powders were evacuated prior to heating to $\approx 6 \times 10^{-2}$ Pa within the vacuum-tight thermal analyzer to remove adsorbed water. During the measurements a flow of 20 ml/min Ar (99.999% purity) was maintained.

3. Results

Fig. 1 shows the DSC curves measured with the c_p-DSC/TG sample carrier for YF_3 and GdF_3 and a DSC curve for one intermediate composition measured with a standard DSC/TG sample carrier. All curves show a first peak that is due to the solid phase transformation of the substances and a second peak due to melting. The fusion point T_f of a pure substance is the extrapolated onset of the melting peak [14], similarly the temperature of a first order solid phase transformation T_t can be obtained from T_{onset} of the transformation peak.

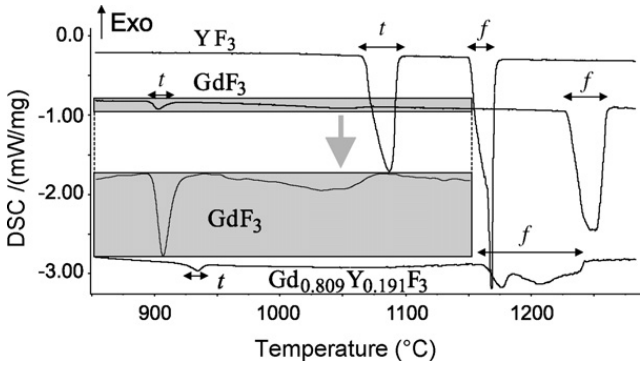

Fig. 1. DSC heating curves obtained from the second heating of YF_3, GdF_3, and of a solid solution $Gd_xY_{1-x}F_3$ ($x = 0.8090$) showing the subsequent phase transformation (t) and fusion (f) peaks. The inset shows the GdF_3 curve for $850\,^{\circ}C \leq T \leq 1150\,^{\circ}C$ with larger scaling for DSC.

Mixed crystals do not show a sharp T_f but a melting range that is defined by the difference between *liquidus* and *solidus* in the $x - T$ phase diagram. The *solidus* can again easily be obtained from T_{onset}, but the determination of T_{liq} from DSC data is not so straightforward. In this work it was found that the expression

$$T_{liq} = T_{sol} + \Delta T(x) - \Delta T(0) \tag{2}$$

gives reasonable values, if $\Delta T(x) = T_{offset} - T_{onset}$ is the width of the melting peak at the intermediate composition $0 < x < 1$ and $\Delta T(0)$ is the weighted (for x) width of the melting peaks for the pure end members.

From the thermodynamic point of view it makes no difference whether melting (*sol* ↔ *liq*) or another first order phase transformation (*high-T* ↔ *low-T*) takes place. Hence, in analogy with the 2-phase-region *high-T* /*liquid* upon melting, a 2-phase-region with the *low-T* and the *high-T* phase will occur. The phase boundaries can be determined from the width of the phase transformation peak similar to (2). The lower boundaries of the two 2-phase-regions in the YF_3–GdF_3 phase diagram (Fig. 2) could be obtained from the $T_{onset}(x)$ of the phase transformation and melting peaks, with typically ±5 K reproducibility. The higher boundaries were obtained from the width of the peaks (2).

4. Discussion

The experimental points (circles and crosses in Fig. 2) show the expected topology of the phase diagram with extended regions for the *low-T*, *high-T*, and *liquid* solution phases. All three phases $Gd_xY_{1-x}F_3$ show complete

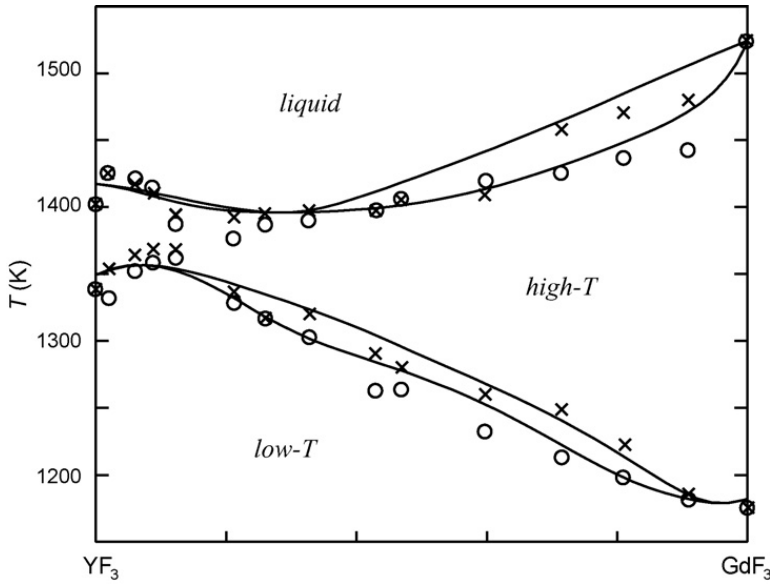

Fig. 2. Experimental points for the phase diagram YF_3–GdF_3 (circles: extrapolated onsets, crosses: calculated from peak width using (2) together with a thermodynamic assessment).

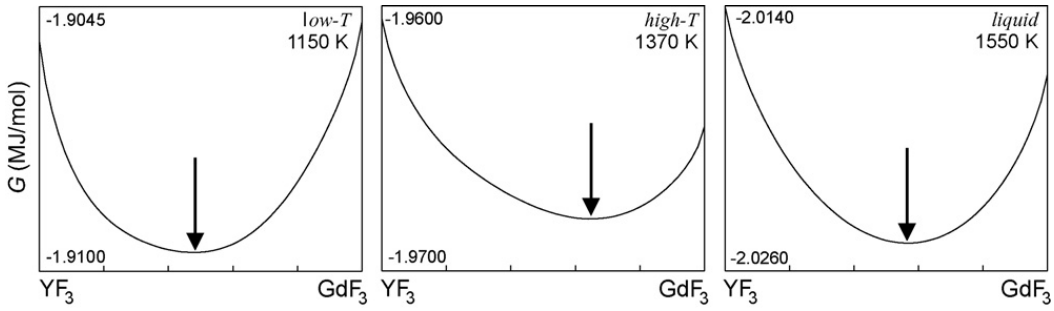

Fig. 3. Gibbs free energy G for $Gd_xY_{1-x}F_3$ in the three phases *low-T* (at $T = 1150$ K), *high-T* (at 1370 K), and *liquid* (at 1550 K). Arrows indicate the minima.

solubility for $0 \leq x \leq 1$, but deviations from ideal solutions are obvious. The minimum of *liquid* around $x \approx 0.25$ and the maximum of *low-T* around $x \approx 0.10$ lead to a narrow *high-T* region for small x (only $\approx$20–30 K). Actually, the width of the DSC peaks (cf. Fig. 1) exceeds the width of the *high-T* region for small x. The phase transformation and melting peaks overlap partially leading to larger experimental errors for $0.1 < x < 0.4$. Moreover, in this composition range the phase transformation and melting processes are extended over a broader T range due to the wide 2-phase regions. The wide 2-phase regions may lead to segregation and thus to different T_p and T_f in different parts of the sample.

A thermodynamic assessment of the phase diagram was performed with the ChemSage [15] PC program. The SUBI model (independent mixing of cations and anions) was used for both solid phases and RKMP (Redlich–Kister–Muggianu) polynoms were used for *liquid* [15,16]. The agreement between the assessment results (lines in Fig. 2) and the experimental data is fairly good, as the remaining differences do not exceed the experimental scatter and as the main features (minima and maxima of the *liquid* and *low-T* regions) are reproduced well.

With the thermodynamic data file that was obtained by assessment one can calculate the Gibbs free energy G for the three solution phases. Fig. 3 shows $G(x)$ for such T, where only one phase is stable for all x. For all phases $G(x)$ has a minimum for intermediate x, but for *high-T* this minimum is most distant from the center near $x = 2/3$, indicating the pronounced stability of *high-T* at large x.

Surprisingly, even the fundamental thermodynamic data for the pure end members of the phase-diagram were found to be different from values contained in thermodynamic databases. The ChemSage program [15] that was available for this study relies on the compilation by Barin [17]. The Barin data are compared with the present results in Table 1. For YF_3 the enthalpy of phase transformation ΔH_p has approximately the same magnitude as the enthalpy of fusion ΔH_f. However, T_p differs by 11 K and T_f by 25 K. Basically one could regard the Barin values as more reliable, as these data are thoroughly cross-checked. Otherwise one should keep in mind that the present results were obtained by measurements with two different sample holders that were calibrated repeatedly prior to and after the measurements with YF_3 and GdF_3. One calibration point was the melting of gold at $T_f = 1336$ K [18] which is very close to T_p of YF_3, thus ensuring high reliability near this point.

Discrepancies are much more pronounced for T_p of GdF_3: Barin and this work differ by more than 170 K! This difference cannot be explained by simple experimental errors. The DSC curve in Fig. 1 clearly shows the transformation peak at 901.7 ° C (1174.8 K); one must assume that the Barin data are erroneous in this point. However, a small endothermal effect around 1060 ° C (1333 K) is also visible in Fig. 1. It seems possible that this

Table 1
Comparison of solid state phase transformation and fusion data for YF_3 and GdF_3 (this work and Barin [17])

	YF_3		GdF_3	
	This work	Barin	This work	Barin
T_p (K)	1338.6	1350.0	1174.8	1348.0
ΔH_p (kJ/mol)	21.138	32.468	9.195	6.004
T_f (K)	1403.1	1428.0	1525.7	1505.0
ΔH_f (kJ/mol)	29.789	27.970	67.612	52.426

Table 2
Fitting parameters for the c_p expression (3)

T-range (K)	c_1	c_2	$c_3 \times 10^3$	$c_4/10^7$	c_5	Phase
YF_3						
300–1246.9	922.13	−14.041	−1.3084	−1.1815	2.1107	*Low-T*
1247.0–1403.2	133.35	0	0	0	0	*High-T*
1403.3–1600.0	138.60	0	0	0	0	*Liquid*
GdF_3						
300–1154.7	−163.59	0.4797	−0.1826	1.11374	0	*Low-T*
1154.8–1333.0	3120.88	−5.1795	2.2615	0	0	*High-T*
1333.1–1525.8	785.92	−0.9768	0.3996	0	0	*High-T*
1525.9–1600.0	176.73	0	0	0	0	*Liquid*

small effect was considered to be the result of a phase transformation by Barin. Indeed, the λ shaped maximum of $c_p(T)$ might be the result of a further and not yet reported second order solid phase transformation of GdF_3.

The specific heat capacity c_p for the three phases of YF_3 and GdF_3 were fitted to equations

$$c_p = c_1 + c_2\,T + c_3\,T^2 + \frac{c_4}{T^2} + c_5\,T\ln T \tag{3}$$

with fitting parameters c_i that are given in Table 2.

Fig. 4 compares the Barin c_p data for GdF_3 with the values that were obtained in this work with powder samples. At least for the *low-T* phase the values are similar around 100 J/mol K, but the present values depend stronger on *T*. For *high-T* and *liquid* Barin gives only constant values of 130.855 or 127.821 J/mol K, respectively. In this work, the *liquid* data scatter around 177 J/mol K and the *high-T* data show a λ-shaped maximum at 1333 K that is responsible for the flat minimum of the GdF_3 DSC curve in Fig. 1. This λ peak might indicate an additional phase transformation (second order) without apparent latent heat. In Table 2 the λ shaped peak of $c_p(T)$ visible in Fig. 4 is described by two sets of $c_i(i = 1, 2, 3)$ parameters for the *high-T* phase of GdF_3.

The Barin compilation [17] is based on experimental data for 10 different REF_3 that were obtained by Spedding et al. [19] using DTA (for T_p and T_f) and drop calorimetry (for c_p). No original DTA curves were reported by these authors and thus the comparison with the present and with Thoma's [20] contradicting results is not possible. It should be noted, however, that Spedding et al. measured oxygen contaminations of their different REF_3 samples ranging from 1 to >300 ppm. Unfortunately, only for GdF_3 no oxygen content data were given.

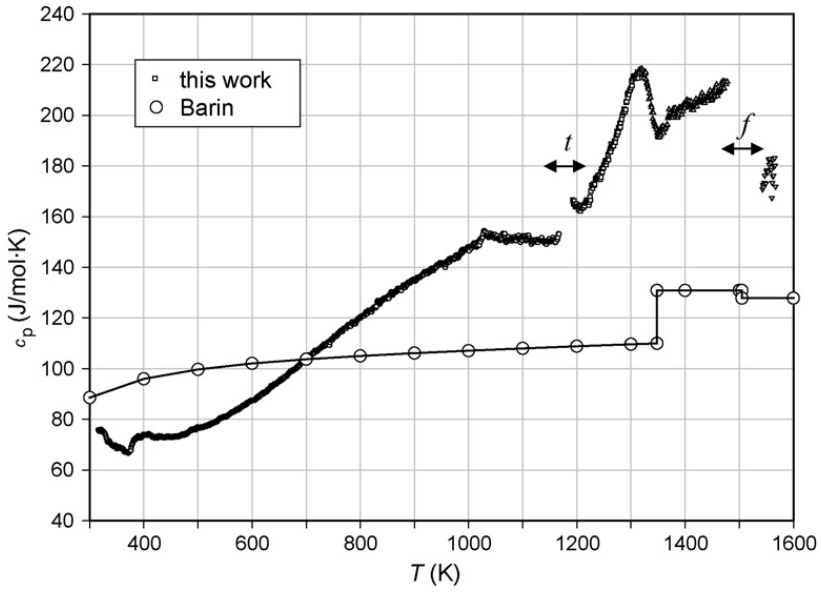

Fig. 4. Specific heat capacity c_p of GdF_3: comparison of data from Barin [17] and from this work.

Different rare earth oxyfluorides REOF and $RE_4O_3F_6$ can undergo phase transformations that are marked by DTA signals with peak temperatures (no onsets are reported) down to 613 ° C (GdOF) or 560 ° C (YOF) [21–23]. The high conversion rates $\gg 99.9\%$ that could be obtained during our REF_3 preparation process assures that such oxyfluoride contamination is not relevant in the samples used in this study.

5. Conclusions

Like most other rare earth fluorides, $GdF_3$and YF_3 undergo upon heating a first order solid phase transformation before melting. GdF_3 and YF_3 show complete miscibility in all three phases *low-T*, *high-T*, and *liquid* and corresponding ''one phase regions'' can be found in the binary phase diagram. The one phase regions are separated by two phase regions *low-T /high-T* and *high-T /liquid*.

In this paper, the first order phase transformation of GdF_3 was found to occur at 902 °C, in contrast to some published data [15,17] that report a much higher transformation temperature (1075 °C), but in agreement with a recent paper by some of us [8]. It should be noted, however, that the present value is in close agreement with the older results of Thoma and Brunton [20]. These authors prepared GdF_3 with < 300 ppm oxygen content from commercial Gd_2O_3 by hydrofluorination with ammonium bifluoride $NH_4F \cdot HF$. Thoma and Brunton determined the phase transformation by X-ray diffraction within high-vacuum better 4.5×10^{-4} Pa. This technique measures directly the changing crystal structure and is not influenced by parasitic thermal effects that might result from chemical reactions between sample and impurities. Therefore, the determination of the orthorhombic/hexagonal phase transformation is expected to be highly reliable in [20].

Acknowledgements

The authors acknowledge financial support by the Deutscher Akademischer Austauschdienst (DAAD, PROBRAL grant D/05/30364) and by the Coordenação de Aperfeiçoamento de Pessoal de Nível Superior (CAPES, PROBRAL grant Nr. 246/06).

References

[1] B.P. Sobolev, I.D. Ratnikova, P.P. Fedorov, Mater. Res. Bull. 11 (1976) 999–1004.
[2] R.C. Pastor, M. Robinson, Mater. Res. Bull. 9 (1974) 569–578.
[3] O. Greis, M.S.R. Cader, Thermochim. Acta 87 (1985) 145–150.
[4] S. Stankus, R.A. Khairulin, K.M. Lyapunov, J. Alloys Compd. 290 (1999) 30–33.
[5] K. Lyapunov, A. Baginskii, S. Stankus, J. Alloys Compd. 372 (2004) 7–9.
[6] W. Korczak, P. Mikołajczak, J. Cryst. Growth 61 (1983) 601–605.
[7] K. Shimamura, E.G. Víllora, S. Nakakita, M. Nikl, N. Ichinose, J. Cryst. Growth 264 (2004) 208–215.
[8] I.M. Ranieri, A.H.A. Bressiani, S.P. Morato, S.L. Baldochi, J. Alloys Compd. 379 (2004) 95–98.
[9] J.S. Abell, I.R. Harris, B. Cockayne, J. Mater. Sci. 12 (1977) 670–674.
[10] I.R. Harris, H. Safi, N.A. Smith, M. Altunbas, B. Cockayne, J.G. Plant, J. Mater. Sci. 18 (1983) 1235–1243.
[11] H. Guggenheim, J. Appl. Phys. 34 (1963) 2482–2485;
see also: R. Bougon, J. Ehretsmann, J. Portier, A. Tressaud, P. Hagenmuller, Preparative Methods in Solid State Chemistry, Academic Press, New York, 1972, p. 401.
[12] I.M. Ranieri, Ph.D. thesis, IPEN/University of São Paulo (2001).
[13] D. Klimm, Thermochim. Acta 339 (1999) 111–116.
[14] G. Höhne, W. Hemminger, H.-J. Flammersheim, Differential Scanning Calorimetry, Springer, Berlin Heidelberg, 1996.
[15] GTT Technologies, Kaiserstr. 100, 52134 Herzogenrath, Germany, ChemSage 4.20, http://www.gtt-technologies.de/(2000).
[16] M. Hillert, B. Jansson, B. Sundman, J. Ågren, Metall. Trans. A 16 (1985) 261–266.
[17] I. Barin, Thermodynamic Data of Pure Substances, VCH, Weinheim, 1993.
[18] GTT Technologies, Kaiserstr. 100, 52134 Herzogenrath, Germany, FactSage 5.4.1, http://www.factsage.com/ (2006).
[19] F.H. Spedding, B.J. Beaudry, D.C. Herderson, J. Moormann, J. Chem. Phys. 60 (1974) 1578–1588.
[20] R.E. Thoma, G.D. Brunton, Inorg. Chem. 5 (1966) 1937–1939.
[21] B.P. Sobolev, P.P. Fedorov, D.B. Shteynberg, B.V. Sinitsyn, G.S. Shakhkalamian, J. Solid State Chem. 17 (1976) 191–199.
[22] K. Niihara, S. Yajima, Bull. Chem. Soc. Japan 44 (1971) 643–648.
[23] K. Niihara, S. Yajima, Bull. Chem. Soc. Japan 45 (1972) 20–23.